

Journal of Materials Chemistry A

Accepted Manuscript



This is an *Accepted Manuscript*, which has been through the Royal Society of Chemistry peer review process and has been accepted for publication.

Accepted Manuscripts are published online shortly after acceptance, before technical editing, formatting and proof reading. Using this free service, authors can make their results available to the community, in citable form, before we publish the edited article. We will replace this *Accepted Manuscript* with the edited and formatted *Advance Article* as soon as it is available.

You can find more information about *Accepted Manuscripts* in the [Information for Authors](#).

Please note that technical editing may introduce minor changes to the text and/or graphics, which may alter content. The journal's standard [Terms & Conditions](#) and the [Ethical guidelines](#) still apply. In no event shall the Royal Society of Chemistry be held responsible for any errors or omissions in this *Accepted Manuscript* or any consequences arising from the use of any information it contains.

ARTICLE

Cite this: DOI: 10.1039/x0xx00000x

Received 00th January 2012,

Accepted 00th January 2012

DOI: 10.1039/x0xx00000x

www.rsc.org/

Monolithic nitrogen-doped graphene frameworks as ultrahigh-rate anodes for lithium ion batteries

Xilai Jia,^{a*} Guolin Zhang,^a Tihong Wang,^a Xiao Zhu,^a Fan Yang,^a Yongfeng Li,^a Yunfeng Lu,^{c*} and Fei Wei^{b*}

Three-dimensional (3D) nanocarbon architectures have attracted great interest in material science and nanotechnology. In this work, we report the synthesis of 3D nitrogen-doped graphene nanoarchitecture by using catalytic carbonization of aromatic polyimide (PI) on magnesium oxide (MgO) nanowires. The produced porous graphene nanofibers are crosslinked into integrated monolithic structure, thereby offering continuous electron conductivity and efficient charge transport. Moreover, nitrogen doping was achieved during the *in-situ* carbonization, enhancing the electronic and interfacial properties of the porous graphene nanofibers. The obtained monolithic frameworks were directly used as binder-free electrodes of lithium batteries, and yield remarkable electrochemical performances, such as high reversible capacity, high rate capability, and superb cycling stability. The monolithic structure can be used as a material platform for preparation of other functional composites, extending their applications beyond energy storage.

Introduction

Lithium ion batteries (LIBs) with higher power densities and better Coulomb's rates (C-rates) are in great demand in many critical applications such as electric vehicles (EVs), smart grids, and renewable energy storage.^{1,2} Traditionally, graphite and other kinds of carbons are widely used as anode materials in current LIBs.^{3,4} However, those carbon materials have inefficient rate capability, and always suffer from low capacities at rapid charge and discharge rates. Therefore, developing high-rate electrode materials with featured improvement of power performance has been an essential component of the current energy storage techniques.^{5,6}

One key design to improve the rate performance of carbon anodes lies in the improvements of charge transports of electrode materials. In this context, electrode materials with low-dimensional properties and 3D porous structuring on those

materials have attracted a lot of attentions,⁷⁻¹² and achieve great enhancement in energy storage. Among those efforts, porous carbon nanofibers have attracted great attention because of their oriented long-range conductivity and facile electrolyte accesses.¹³⁻¹⁷ For example, high-rate electrodes of carbon nanofibers were fabricated from carbonization of spined polymer nanofibers,^{18,19} which leads to the electrodes with better rate capability and cycling stability than most carbon anodes. Nevertheless, if the strategies of pore structuring are not well designed, the polymer nanofibers may be of low surface areas, leading to their electrodes with unexpectedly low rate performance. B. Zhang et al reported the synthesis of porous graphitic carbon nanofibers by incorporating sacrificed precursor for pore-forming,²⁰ and demonstrated high-rate performance as battery anode materials. The performance, however, could be further enhanced provided that the contacts between the nanofibers could be crosslinked to form network structure, since more and more efforts on 3D nanocarbon electrodes have shown that such crosslinked networks can bring on continuous conductive pathways and better structure properties than single low-dimensional nanocarbons.²¹⁻²³

To further enhance the electrochemical performance of carbon anodes, introduction of heteroatoms into carbon frameworks are used to tailor the electronic and interfacial properties of carbon materials.²⁴⁻²⁷ Among the efforts, nitrogen (N)-doping strategies such as *in-situ* preparation of N-doped carbons during their preparation processes²⁸⁻³⁰ and post treatment of carbon materials in the presence of nitrogen source³¹⁻³³ are proved to be effective methods, which endow their

^aState Key Laboratory of Heavy Oil Processing, China University of Petroleum, Beijing, Changping 102249, P. R. China. E-mail: jiaxily@gmail.com

^bBeijing Key Laboratory of Green Chemical Reaction Engineering and Technology, Department of Chemical Engineering, Tsinghua University, Beijing 100084, People's Republic of China. E-mail: wf-dce@tsinghua.edu.cn

^cDepartment of Chemical and Biomolecular Engineering, University of California, Los Angeles, California 90095, United States. E-mail: lucla@ucla.edu

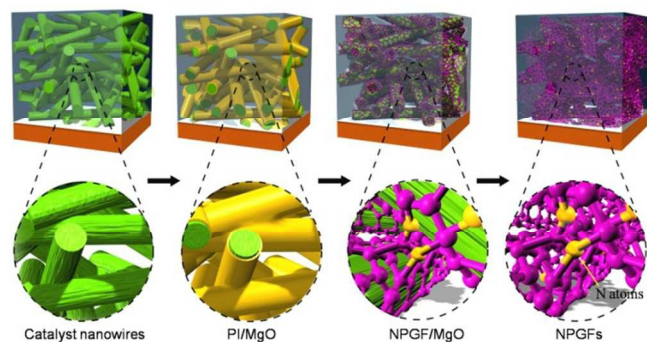
†Electronic Supplementary Information (ESI) available: Additional data.

anodes with better rate performance than the pristine ones. However, those methods may result in a low content of nitrogen, or unstable doping of heteroatoms in some cases. To circumvent this problem, pyrolysis of nitrogen-containing polymers^{23,34} or other compounds³⁵ can introduce the nitrogen atoms into the carbon frameworks with durable properties. Although great efforts on N-doped carbon materials have been reported for energy storage, 3D nanocarbon architectures with tailored porosity and enhanced electric conductivity are still highly desirable.

In this work, we report the fabrication of 3D N-doped porous graphene frameworks (NPGFs) based on catalytic carbonization process. The products are monolithic films that can be directly used as binder-free anodes with superior rate capability and cycling stability. Scheme 1 illustrates the synthesis route towards the monolithic nanocarbon architecture. We started with synthesis of magnesium oxide (MgO) precursor nanowires that are filtrated into free-standing films. Subsequently, the films were incorporated into the precursors of PI to serve as both the catalyst for graphene and the sacrificial phase for creating pores. The adsorbed PI precursors were polymerized and used as carbon sources that were further converted into N-doped graphene after carbonization at 900 °C under argon (Ar) atmosphere. After removing the templates using acid washing, porous monolithic films consisting of crosslinked N-doped graphene nanofibers were obtained. As used for energy storage, the monolithic frameworks provide the key features required for high-rate electrodes:

1. Effective transport of electrons and ions. The conductivity of such electrodes is provided by 3D networks consisting of crosslinked graphene nanofibers, and further enhanced by *in-situ* doping of nitrogen atoms. The interconnected networks of the electrodes and the porous structure of the nanofibers provide facile electrolyte transport and kinetically rapid ion diffusion during the charge-transfer processes.

2. Integrated 3D structure. As the frameworks are built from crosslinked graphene nanofibers, the electrodes have robust pathways for charge transports during charge/discharge processes, thereby offering durable performance.



Scheme 1 Evolution of nitrogen-doped graphene frameworks: A) free-standing catalyst film of MgO precursor nanowires; B) PI/MgO nanocomposite by coating catalyst nanowires using aromatic polyimide; C) N-doped graphene/MgO nanocomposite after catalytic carbonization process; and D) monolithic N-doped graphene film after removing MgO component.

Experimental

Materials

Magnesium acetate, urea, pyromellitic dianhydride (PMDA), and 4,4'-oxydianiline (ODA) are analytical reagent (AR), and purchased from Shanghai Chemicals Co. (Shanghai, China). N,N-Dimethylacetamide (DMAc, AR) was purchased from Beijing Chemicals Co. (Beijing, China). All chemicals were used as received.

Synthesis of N-GF films

MgO precursor nanowires was prepared using a hydrothermal method.³⁶ The catalyst nanowires were dispersed into suspension of 3.0 g L⁻¹, and were filtered to form films with different thicknesses. The films were dried under vacuum at 120 °C for 24 h before use. 0.5010 g of ODA was dissolved into 30 ml of DMAc by stirring for 50 min, into which was then added 0.5568 g of PMDA. After reaction of 1 h under N₂, viscous PMDA-ODA polyamic acid (PAA) mucus was produced. The viscous PAA mucus was diluted into a solution of 0.015 g mL⁻¹ for use.³⁷ After that, PAA was absorbed into the catalyst film of MgO precursor nanowires, and treated at 300 °C for 2 h in Ar, resulting in MgO/PI nanocomposites. Then, the MgO/PI nanocomposites were carbonized at 900 °C for 2 h under Ar of 100 mL min⁻¹. The products were soaked using 12 wt% acid HCl for three times, washed with water, and dried at 300 °C for 1 h to obtain the free-standing NPGFs.

Characterization

SEM experiments were conducted on a JEOL JSM-6700 FE-SEM. TEM experiments were conducted on a JEM-2010 instrument operated at 120 kV. X-ray diffraction was conducted on a BRUKER D8 ADVANCE X-ray powder diffractometer using Cu-K α radiation ($\lambda=1.54$ Å). Nitrogen sorption isotherms were measured at 77 K with a Micromeritics ASAP 2020 analyzer. The specific surface areas were calculated by using adsorption branch in a relative pressure range from 0.04 to 0.25. The pore size distributions were derived from the adsorption branch of isotherms using the Barrett-Joyner-Halenda (BJH) model. The surface composition of cross-linked composite was analyzed by X-ray photoelectron spectroscopy (XPS) with a PHI 3057 spectrometer using Mg-K X-rays at 1253.6 eV. Raman spectra were performed on a Horiba Jobin Yvon Lab RAMHR800 Raman spectrometer with He-Ne laser excitation at 633 nm. The Fourier transform infrared (FT-IR) spectra were collected with a Magna-IR 560 E.S.P spectrometer. Thermalgravimetric analysis (TGA) of MgO/PI was conducted on a STA7200 (HITACHI) instrument.

Electrochemical characterizations

To test the electrochemical performance, NPGF films were cut into desired sizes, and were then assembled into 2032-type coin cells, where glass fibers (Whatman) were used as the separators and lithium foils were used as both the counter and reference electrodes. The electrolyte solution was a 1 mol L⁻¹ LiPF₆ in ethylene carbonate (EC)/diethyl carbonate (DEC) (1:1 by

volume) solution. The mass loading of NPGF electrodes of 80 μm is 0.3 mg cm^{-2} . The cells were assembled in a glove box under an argon atmosphere. CV measurements and electrochemical impedance spectroscopy (EIS) tests of the cells were carried out on a CHI 660C electrochemical workstation. The galvanostatic charge/discharge measurements were carried out by a LAND CT2000 battery tester at various current densities.

Results and discussion

Fig. 1A and B showed the catalyst film consisting of MgO precursor nanowires, and the prepared free-standing NPGF film. The structure and morphology evolution during the formation of N-doped graphene was investigated using electron microscopic techniques, infrared spectroscopy, and thermogravimetric analysis. Scanning electron microscopy (SEM) observation of catalyst film reveals that it was composed of random nanofibers with the diameters ranging at hundreds of nanometers (Fig. S1A). Transmission electron microscopy (TEM) image reveals that interconnected pores exist within in the nanowires (Fig. S1B), which facilitate the access of PI precursors. When the precursors were adsorbed in the networks and nanowires, they will form robust composite films after polymerization. This coating strategy is very important for preparing the monolithic frameworks, because the nanowire films may be easily broken down if they are directly put in a high temperature of ca. $900 \text{ }^\circ\text{C}$. Based on our processes, the produced films are flexible in a certain degree, and can be tailored into desired sizes (Fig. 1C). The thickness of the monolithic films can be readily tuned depending on that of catalyst films (Fig. S2). Their electric conductivities were 33 S m^{-1} (Fig. S3). Compared with some reported nanocarbon frameworks,^{38,39} the NPGF film is less conductive. Considering the highly porous structure, however, this conductivity value is good. The synthesis process was monitored using infrared spectroscopy (Fig. 1D). The peaks of PI and catalyst nanowires disappeared in the products, while the characteristic peaks of C=C, C=N, and C=O become obvious at $1620\text{--}1720 \text{ cm}^{-1}$, suggesting that PI was successfully converted into carbon materials with hybrid atoms.⁴⁰ In addition, TGA of the catalytic carbonization process of PI/MgO composite films indicated that the conversion ratio of PI into NPGF was 40 wt% in this process (Fig. 1E).

Fig. 2A shows the SEM image of produced monolithic films. The films are composed of nanofiber networks. The diameters of the nanofibers are comparable to that of MgO nanowires. The nanofibers show high lengths, and more importantly, are interweaved into web-like structure, with no obvious morphology breakdown (Fig. 2B). Accordingly, cross-sectional view of the film shows that the graphene nanofibers are crosslinked into an integrated film (Fig. 1C). The contacts between nanofibers are highly crosslinked, not in an isolated state (Fig. 1D). The structure was further conformed by low-magnification TEM observation (Fig. 2E), where the crosslinks between nanofibers are bonded together to form robust contacts. The intimate contacts endow the whole monolithic frameworks with 3D continuous networks that are desired for efficient charge transport of electrodes. Moreover, close observation of the nanofibers shows that abundant mesopores with averaged diameter of $\sim 5.0 \text{ nm}$ are formed in the building nanofibers (Fig. 2F). Such mesoporous structure will shorten the ion diffusion lengths of electrode materials. Note that

nitrogen doping was achieved by *in-situ* process. The uniform doping will further enhance the electrical conductivity, and improve the interfacial properties of electrodes.

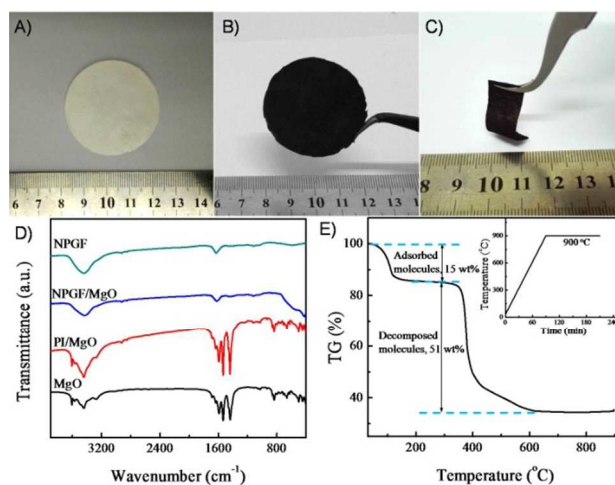


Fig. 1 Photographs of self-supported A) MgO precursor nanowire, and B) NPGF films. C) Photograph of bent NPGF film. D) FT-IR of MgO nanowires, PI/MgO composite, NPGF/MgO composite, and NPGF. E) TGA of the catalytic carbonization process of PI/MgO composite films (the conversion ratio of PI into NPGF = $(100\% - 15\% - 51\%) / (100\% - 15\%) = 40 \text{ wt}\%$).

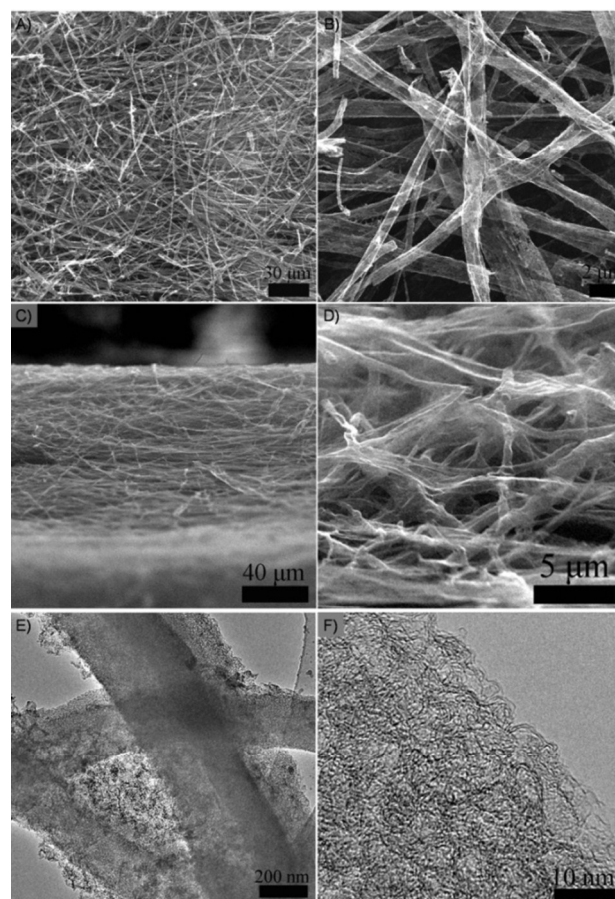


Fig. 2 SEM images of NPGF films under A, B) frontal and C, D) cross-sectional observation. E, F) TEM images of NPGF films.

Fig. 3A shows the survey-scan X-ray photoelectron spectroscopy (XPS) spectrum of NPGF films, where the characteristic peaks of nitrogen, oxygen and carbon are observed at 284, 400, and 532 eV respectively. The nitrogen content was calculated to be 2.6 wt-%. The high-resolution N1s spectrum of the nanofibers can be deconvoluted into two peaks at 398.1 and 400.2 eV, respectively (Inset of Fig. 3A). The dominant peak of 400.2 eV was ascribed to quaternary nitrogen; while the small peak at 398.1 eV is attributed to the presence of pyridinic nitrogen.¹⁸ Moreover, the existence of oxygen (10.1 wt-%) could be ascribed to the abundant edges of the porous structure, which was also observed in most porous graphene.⁴¹ The introduction of hybrid atoms and the porous structure introduce great disorder of graphene. Therefore, XRD pattern of NPGFs show broad peaks at about 29.7 and 41.9° (Fig. 3B), consistent with previously reported porous carbons.⁴² Raman spectrum of the films exhibited two typical peaks around 1326 and 1591 cm⁻¹, which are attributed to the well-defined D band and G band, respectively (Fig. 3C). The intensity ratio of the G to the D band is 0.8, which is characteristic of graphitic carbons with a defective structure.⁴³ In addition, the pore structure of the frameworks was characterized using nitrogen-sorption measurement (Fig. 3D). The sorption isotherm curve of the frameworks shows the absence of adsorption-desorption hysteresis, preferably corresponding to type II isotherm. The frameworks have a moderate Brunauer-Emmett-Teller (BET) surface area of 610 m² g⁻¹, and a pore volume of 0.745 m³ g⁻¹. Analysis of the pore-size distribution (inset of Fig. 3D) indicated that the pores of the films were hierarchically structured mesopores averaged at 4.9 nm, well consistent with TEM observation. Such hierarchically structured pores enable facile electrolyte transports, key for the electrode's rate performance.

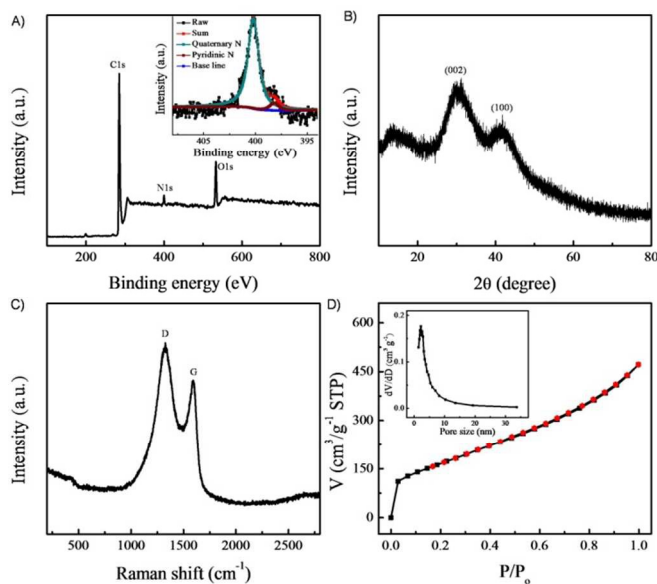


Fig. 3 A) XPS spectrum (Inset, high-resolution spectrum of the N1s peak), B) XRD pattern, C) Raman spectrum, and D) nitrogen adsorption-desorption isotherm and BJH pore-size distribution (inset) of the NPGF films.

Owing to the structure features, the binder-free electrodes of NPGFs exhibit durable energy-storage performance. Cyclic

voltammetry (CV) is first used to investigate their lithium storage behavior (Fig. 4A). In the first cycle, an irreversible capacity loss at 0.63 V was observed, which was ascribed to the irreversible reduction of electrolyte and solid electrolyte interphase (SEI) formation.⁴⁴ However, redox reactions of lithium insertion/extraction were highly reversible in the subsequent cycles. The lithium removal occurs over a broad potential range, different from graphite that usually significant peaks below 1.0 V.⁴⁵ The broad features suggest continuous charge-transfer processes of the electrode materials. At a current density of 200 mA g⁻¹, the initial charge and discharge cycle delivered specific capacities of 1452.0 and 758.9 mAh g⁻¹ respectively (Fig. 4B), followed by the reversible capacity around 700 mAh g⁻¹ at the voltage of 0.005-3 V. The reports achieving capacities more than 300 mAh g⁻¹ for carbon anodes are typically obtained at much lower current densities than that reported here.^{46,47} For more practical application, the cells were tested at voltage range of 0.005-2 V at various current densities (Fig. 4C). Even at increasing the current densities, charge-discharge storage behaviors are well maintained.

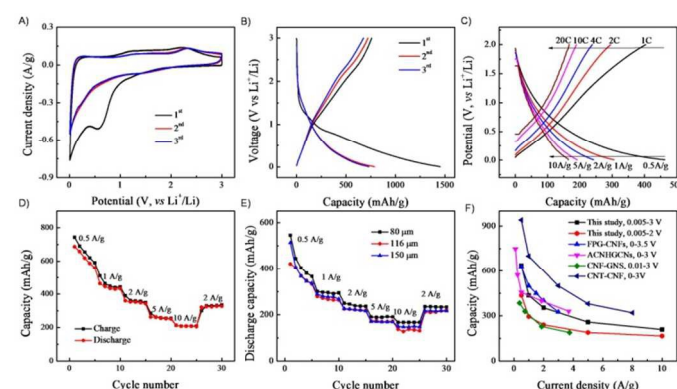


Fig. 4 A) CV plots of NPGF electrode at the first three cycles at a sweep rate of 0.1 mV s⁻¹. B) Charge/discharge curves of the electrodes at a current density of 200 mA g⁻¹. C) Charge/discharge curves of the electrodes at various current densities from 0.5 to 10 A g⁻¹. D) Rate performance of the electrode at 0.005-3 V. E) Rate performance of the electrodes with various thicknesses of 80, 116, and 150 μm between 0.005 and 2 V. F) Rate performance comparison of NPGF electrodes with reported typical carbon anodes.

Most carbon anodes suffer from high-rate performance. Herein, the prepared NPGF electrodes demonstrate excellent rate capability (Fig. 4D). The capacities of the total electrodes were ~640 mAh g⁻¹ at a current density of 0.5 A g⁻¹ at 0.005-3 V. Consistent with initial charge/discharge curves, the capacity degrades slowly after 5 cycles at this rate. Nevertheless, after the initial drop, reversible capacities of 435, 356, and 258 mAh g⁻¹ are attained at current densities of 1, 2, and 5 A g⁻¹ respectively. Even at super high current rate of 10 A g⁻¹, the electrode delivered a reversible capacity of 210 mAh g⁻¹, demonstrating the remarkable rate performance. Moreover, it is essential, but challenging, to make thick electrodes (e.g., >100 μm) towards high-performance devices. Herein, electrodes with various thicknesses of 80, 116 and 150 μm were prepared and compared in coin-cells (Fig. 4E). The electrodes show almost the same rate capacities, suggesting well-maintained rate performance. The rate performance of such NGF electrodes was excellent and comparable to that of reported typical carbon anodes (Fig. 4F), such as

functionalized porous carbon nanofibers (FPG-CNFs, tested in 0-3.5 V),²⁰ amorphous carbon nanotubes decorated with hollow graphitic carbon nanospheres (ACNHGCNs, 0-3V),⁴⁶ carbon nanofiber/graphene hybrids (CNF-GNS, 0.01-3 V),⁷ activated N-doped hollow carbon nanotube/carbon nanofiber composites (CNT-CNF, 0-3 V),⁴⁹ and other porous carbons.^{31,50-52} The improved storage properties are associated with improved transport in the hierarchically porous structure of the electrodes, and, more importantly, increased conductivity due to the formation of crosslinked N-doped graphene networks. The design of such integrated graphene frameworks can provide an available material for high-rate electrode materials.

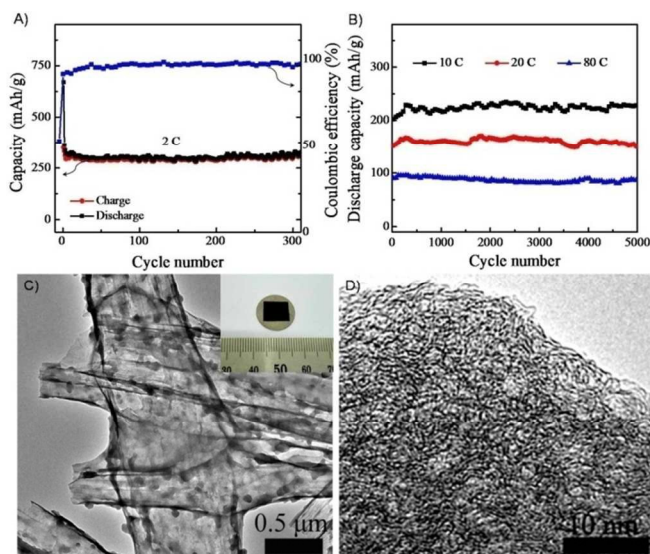


Fig. 5 A) Cycling stability and the coulombic efficiency of NPGF electrodes at the rate of 2 C. B) Long-term cycling stability at the high rates of 10, 20, and 80 C. C) and D) TEM images of the NPGF electrode after 5000 cycles at the rate of 10 C (Inset is the digital photograph of the electrode after 5000 cycles).

The stability of the electrodes during charge-discharge cycling was exhibited in Fig. 5. The electrode offered a total discharge capacity of $\sim 300 \text{ mA h g}^{-1}$ at the rate of 2 C in the initial several cycles, and gradually maintained at $\sim 280 \text{ mA h g}^{-1}$ with no obvious capacity fading during 300 cycles. Coulombic efficiency was maintained around 98% upon cycling, supporting the highly reversible electrochemical reaction. For further test the long-term cycling stability at high rates, the electrodes were charged and discharged at the extremely high rates of 10, 20, and 80 C (Fig. 5B). The electrodes displayed superior stability. Moreover, EIS was conducted along with galvanostatic charge/discharge cycles of the electrode at the rate of 10 C (Fig. S4). The Nyquist plots exhibit similar features after the initial cycles, suggesting high cycling stability. To investigate the reason for the high stability, the electrode cycled after the long-term cycles was examined under electron microscopes. The electrode retains its initial crosslinked networks (Fig. 5C), as well as the hierarchically structured pores (Fig. 5D), further confirming its structure robustness.

We notice that graphene nanostructures for energy storage are mostly made from graphene or graphene oxide dispersions.⁵³⁻⁵⁵ This often suffers from dispersion and reassembly, leading to much lower structure robustness. By comparison, the synthesis method here utilized the high-temperature catalytic carbonization, which enables

the films with better structure integrity.⁵⁶ Learning from reported composite synthesis strategies,⁵⁷⁻⁶³ the porous monolithic nanostructure can be loaded with various nanoparticles as a multifunctional supporter, offering a versatile material platform (e.g., TiO_2 used as anodes, Fig. S5). Moreover, as battery electrodes, both the metal current collectors and the polymeric binders are eliminated in such electrodes, increasing the total devices' energy densities.

Conclusions

In summary, we have demonstrated the successful synthesis of hierarchically structured monolithic N-doped graphene nanoarchitecture by using MgO-catalytic carbonization of aromatic polyimide. The 3D nanoarchitecture is composed of crosslinked porous graphene nanofibers, offering long-rang electron conductivity and efficient ion transport, and more importantly integrated robust structure. As directly used as battery anodes, the binder-free electrodes yield remarkable electrochemical performances. The electrodes show high reversible capacity and ultrahigh rate capability. Moreover, durable cycling stability as also attained at both low and high current rates. Considering the structure features, such porous graphene frameworks can be loaded various materials for energy storage, catalyst, sensing, and other applications.

Acknowledgements

This work was supported by Science Foundation of China University of Petroleum, Beijing (No. 2462013YJRC028), and partially supported by National Basic Research Program of China (No. 2011CB932602) and Natural Scientific Foundation of China (No. 21306102).

Notes and references

- P. G. Bruce, B. Scrosati and J. M. Tarascon, *Angew. Chem. Int. Ed.*, 2008, **47**, 2930-2946.
- B. Kang and G. Ceder, *Nature*, 2009, **458**, 190-193.
- I. Lahiri and W. Choi, *Crit. Rev. Solid State Mater. Sci.*, 2013, **38**, 128-166.
- M. Endo, C. Kim, K. Nishimura, T. Fujino and K. Miyashita, *Carbon*, 2000, **38**, 183-197.
- X. Jia, Z. Chen, X. Cui, Y. Peng, X. Wang, G. Wang, F. Wei and Y. Lu, *ACS Nano*, 2012, **6**, 9911-9919.
- X. Jia, X. Zhu, Y. Cheng, Z. Chen, G. Ning, Y. Lu and F. Wei, *Small*, 2015, doi: 10.1002/sml.201403196.
- Z.-J. Fan, J. Yan, T. Wei, G.-Q. Ning, L.-J. Zhi, J.-C. Liu, D.-X. Cao, G.-L. Wang and F. Wei, *ACS Nano*, 2011, **5**, 2787-2794.
- S. Dutta, A. Bhaumik and K. C. W. Wu, *Energy Environ. Sci.*, 2014, **7**, 3574-3592.
- S. L. Candelaria, Y. Shao, W. Zhou, X. Li, J. Xiao, J.-G. Zhang, Y. Wang, J. Liu, J. Li and G. Cao, *Nano Energy*, 2012, **1**, 195-220.
- J. Wang, H. L. Xin and D. Wang, *Part. Part. Syst. Charact.*, 2014, **31**, 515-539.
- L. Dai, D. W. Chang, J.-B. Baek and W. Lu, *Small*, 2012, **8**, 1130-1166.

12. Z. Li, Z. Xu, X. Tan, H. Wang, C. M. B. Holt, T. Stephenson, B. C. Olsen and D. Mitlin, *Energy Environ. Sci.*, 2013, **6**, 871-878.
13. H. He, L. Shi, Y. Fang, X. Li, Q. Song and L. Zhi, *Small*, 2014, **10**, 4671-4676.
14. X.-Q. Zhang, Q. Sun, W. Dong, D. Li, A.-H. Lu, J.-Q. Mu and W.-C. Li, *J. Mater. Chem. A*, 2013, **1**, 9449-9455.
15. L. Fu, K. Tang, K. Song, P. A. van Aken, Y. Yu and J. Maier, *Nanoscale*, 2014, **6**, 1384-1389.
16. L.-F. Chen, X.-D. Zhang, H.-W. Liang, M. Kong, Q.-F. Guan, P. Chen, Z.-Y. Wu and S.-H. Yu, *ACS Nano*, 2012, **6**, 7092-7102.
17. L.-F. Chen, Z.-H. Huang, H.-W. Liang, W.-T. Yao, Z.-Y. Yu and S.-H. Yu, *Energy Environ. Sci.*, 2013, **6**, 3331-3338.
18. Y. Li, J. Dong, J. Zhang, X. Zhao, P. Yu, L. Jin and Q. Zhang, *Small*, 2015, doi: 10.1002/sml.201403575.
19. S.-X. Wang, L. Yang, L. P. Stubbs, X. Li and C. He, *ACS Appl. Mater. Interfaces*, 2013, **5**, 12275-12282.
20. B. Zhang, Z.-L. Xu, Y.-B. He, S. Abouali, M. Akbari Garakani, E. Kamali Heidari, F. Kang and J.-K. Kim, *Nano Energy*, 2014, **4**, 88-96.
21. H. Ji, L. Zhang, M. T. Pettes, H. Li, S. Chen, L. Shi, R. Piner and R. S. Ruoff, *Nano Lett.*, 2012, **12**, 2446-2451.
22. L. Jiang and Z. Fan, *Nanoscale*, 2014, **6**, 1922-1945.
23. L. Qie, W. M. Chen, Z. H. Wang, Q. G. Shao, X. Li, L. X. Yuan, X. L. Hu, W. X. Zhang and Y. H. Huang, *Adv. Mater.*, 2012, **24**, 2047-2050.
24. D. Wei, Y. Liu, Y. Wang, H. Zhang, L. Huang and G. Yu, *Nano Lett.*, 2009, **9**, 1752-1758.
25. Z.-S. Wu, W. Ren, L. Xu, F. Li and H.-M. Cheng, *ACS Nano*, 2011, **5**, 5463-5471.
26. W. H. Shin, H. M. Jeong, B. G. Kim, J. K. Kang and J. W. Choi, *Nano Lett.*, 2012, **12**, 2283-2288.
27. C. Ma, X. Shao and D. Cao, *J. Mater. Chem.*, 2012, **22**, 8911-8915.
28. A. L. M. Reddy, A. Srivastava, S. R. Gowda, H. Gullapalli, M. Dubey and P. M. Ajayan, *ACS Nano*, 2010, **4**, 6337-6342.
29. J. Wei, D. Zhou, Z. Sun, Y. Deng, Y. Xia and D. Zhao, *Adv. Funct. Mater.*, 2013, **23**, 2322-2328.
30. H. Jin, H. Zhang, H. Zhong and J. Zhang, *Energy Environ. Sci.*, 2011, **4**, 3389-3394.
31. X. Li, D. Geng, Y. Zhang, X. Meng, R. Li and X. Sun, *Electrochem. Commun.*, 2011, **13**, 822-825.
32. H. Wang, C. Zhang, Z. Liu, L. Wang, P. Han, H. Xu, K. Zhang, S. Dong, J. Yao and G. Cui, *J. Mater. Chem.*, 2011, **21**, 5430-5434.
33. D. Geng, Y. Chen, Y. Chen, Y. Li, R. Li, X. Sun, S. Ye and S. Knights, *Energy Environ. Sci.*, 2011, **4**, 760-764.
34. H.-G. Wang, Z. Wu, F.-L. Meng, D.-L. Ma, X.-L. Huang, L.-M. Wang and X.-B. Zhang, *ChemSusChem*, 2013, **6**, 56-60.
35. D.-C. Guo, J. Mi, G.-P. Hao, W. Dong, G. Xiong, W.-C. Li and A.-H. Lu, *Energy Environ. Sci.*, 2013, **6**, 652-659.
36. A. A. Al-Ghamdi, F. Al-Hazmi, F. Alnowaiser, R. M. Al-Tuwirqi, A. A. Al-Ghamdi, O. A. Alhartomy, F. El-Tantawy and F. Yakuphanoglu, *J. Electroceram.*, 2012, **29**, 198-203.
37. X. Jia, Q. Zhang, M.-Q. Zhao, G.-H. Xu, J.-Q. Huang, W. Qian, Y. Lu and F. Wei, *J. Mater. Chem.*, 2012, **22**, 7050-7056.
38. J. Liu, L. Zhang, H. B. Wu, J. Lin, Z. Shen and X. W. Lou, *Energy Environ. Sci.*, 2014, **7**, 3709-3719.
39. Z. Chen, W. Ren, L. Gao, B. Liu, S. Pei and H.-M. Cheng, *Nat. Mater.*, 2011, **10**, 424-428.
40. X. Ma, R. Swaidan, B. Teng, H. Tan, O. Salinas, E. Litwiller, Y. Han and I. Pinnau, *Carbon*, 2013, **62**, 88-96.
41. G. Ning, C. Xu, X. Zhu, R. Zhang, W. Qian, F. Wei, Z. Fan and J. Gao, *Carbon*, 2013, **56**, 38-44.
42. L. Zhao, N. Baccile, S. Gross, Y. Zhang, W. Wei, Y. Sun, M. Antonietti and M.-M. Titirici, *Carbon*, 2010, **48**, 3778-3787.
43. G. Ning, Z. Fan, G. Wang, J. Gao, W. Qian and F. Wei, *Chem. Commun.*, 2011, **47**, 5976-5978.
44. S. Flandrois and B. Simon, *Carbon*, 1999, **37**, 165-180.
45. L.-Z. Bai, D.-L. Zhao, T.-M. Zhang, W.-G. Xie, J.-M. Zhang and Z.-M. Shen, *Electrochim. Acta*, 2013, **107**, 555-561.
46. X. Li, J. Liu, Y. Zhang, Y. Li, H. Liu, X. Meng, J. Yang, D. Geng, D. Wang, R. Li and X. Sun, *J. Power Sources*, 2012, **197**, 238-245.
47. S. Yang, X. Feng, L. Zhi, Q. Cao, J. Maier and K. Müllen, *Adv. Mater.*, 2010, **22**, 838-842.
48. Y. Chen, Z. Lu, L. Zhou, Y.-W. Mai and H. Huang, *Energy Environ. Sci.*, 2012, **5**, 7898-7902.
49. Y. Chen, X. Li, K. Park, J. Song, J. Hong, L. Zhou, Y.-W. Mai, H. Huang and J. B. Goodenough, *J. Am. Chem. Soc.*, 2013, **135**, 16280-16283.
50. X. Zhou, J. Tang, J. Yang, J. Xie and B. Huang, *J. Mater. Chem. A*, 2013, **1**, 5037-5044.
51. W. Wang, Y. Sun, B. Liu, S. Wang and M. Cao, *Carbon*, 2015, **91**, 56-65.
52. A. D. Roberts, S. Wang, X. Li and H. Zhang, *J. Mater. Chem. A*, 2014, **2**, 17787-17796.
53. X.-C. Chen, W. Wei, W. Lv, F.-Y. Su, Y.-B. He, B. Li, F. Kang and Q.-H. Yang, *Chem. Commun.*, 2012, **48**, 5904-5906.
54. S. Yin, Y. Zhang, J. Kong, C. Zou, C. M. Li, X. Lu, J. Ma, F. Y. C. Boey and X. Chen, *ACS Nano*, 2011, **5**, 3831-3838.
55. J. H. Lee, N. Park, B. G. Kim, D. S. Jung, K. Im, J. Hur and J. W. Choi, *ACS Nano*, 2013, **7**, 9366-9374.
56. Y. Zhu, L. Li, C. Zhang, G. Casillas, Z. Sun, Z. Yan, G. Ruan, Z. Peng, A.-R. O. Raji, C. Kittrell, R. H. Hauge and J. M. Tour, *Nat. Commun.*, 2012, **3**, 1225.
57. Z.-S. Wu, S. Yang, Y. Sun, K. Parvez, X. Feng and K. Müllen, *J. Am. Chem. Soc.*, 2012, **134**, 9082-9085.
58. X. Zhu, G. Ning, X. Ma, Z. Fan, C. Xu, J. Gao, C. Xu and F. Wei, *J. Mater. Chem. A*, 2013, **1**, 14023-14030.
59. Y. Chen, X. Li, X. Zhou, H. Yao, H. Huang, Y.-W. Mai and L. Zhou, *Energy Environ. Sci.*, 2014, **7**, 2689-2696.
60. B. Wang, X. Li, B. Luo, J. Yang, X. Wang, Q. Song, S. Chen and L. Zhi, *Small*, 2013, **9**, 2399-2404.
61. Z. Chen, Y. Yuan, H. Zhou, X. Wang, Z. Gan, F. Wang and Y. Lu, *Adv. Mater.*, 2014, **26**, 339-345.
62. J. Liu, J. Sun and L. Gao, *J. Phys. Chem. C*, 2010, **114**, 19614-19620.
63. J. Liu, M. Chen, L. Zhang, J. Jiang, J. Yan, Y. Huang, J. Lin, H. J. Fan and Z. X. Shen, *Nano Lett.*, 2014, **14**, 7180-7187.

ToC

Monolithic three-dimensional nitrogen-doped graphene nanoarchitecture was prepared and used as a high-performance binder-free electrode of lithium ion batteries.

